COMMUNICATION

Coordination chemistry of titanium and zinc in $Ti_{(1-x)}Zn_{2x}O_2$ ($0 \leqslant x \leqslant 1$) ultrathin films grown by DC reactive magnetron sputtering

Ignacio Caretti,* Miriam Yuste, Ricardo Torres, Olga Sánchez, Ignacio Jiménez and Ramón Escobar Galindo

XANES and RBS were used to explore the structural phase and composition transitions of ultrathin films with $Ti_{(1-x)}Zn_{2x}O_2$ stoichiometries, from very low (~0.5 at.%) to high (~25 at.%) titanium content. In this way, the coordination chemistry of Ti^{4+} and Zn^{2+} cations was examined for a wide range of oxide compositions.

Transition metal doping and the formation of mixed oxides are widely used mechanisms to improve the intrinsic properties of binary oxides. Both procedures have been decisive in explaining the spectacular increase of applications based on ZnO and TiO_2 films.

Proven applications of metal-doped ZnO in optoelectronic devices include photovoltaic and dye sensitized solar cells, flat panel displays, photodetectors, gas sensors, light emitting diodes and blue laser diodes.[1–4] The vast majority of previous work on doped ZnO films is related to doping with group III elements. In particular Al, Ga and In trivalent cations have been extensively used to enhance the n-type conductivity of ZnO films.[5–11] Fewer studies have been performed on quadrivalent dopants, such as titanium, which have one more valence than the trivalent cations and can provide two free electrons per atom to improve the conductivity of the ZnO host. In particular the Ti^{4+} cation has a slightly smaller radius (6.8 nm) than Zn^{2+} (7.4 nm) and, thus, it can act as a suitable donor in ZnO films. Some authors have reported an enhancement of the conductivity in Ti–ZnO (TZO) films for low titanium content (<1.5 at.%).[12–16] However, the conduction mechanism of the metal–semiconductor transition in Ti-doped ZnO is still unclear.[17–18]

In turn, ZnO–TiO_2 mixed oxides have been widely studied for use as gas sensors,[19–20] antireflective coatings in solar cells,[21–22] in photocatalytic and self-cleaning applications showing an improved photocatalytic activity and an extended absorption threshold towards the visible range[23] and, more recently, as promising candidates for high frequency dielectric materials[24,25] or novel luminescent phosphors.[26] The mechanisms driving the formation of three different zinc titanate compounds in the ZnO–TiO_2 system, namely, zinc *ortho*-titanate Zn_2TiO_4 (cubic inverse spinel crystal structure with a unit cell a = 0.846 nm), zinc *meta*-titanate $ZnTiO_3$ (either cubic inverse defect spinel, a = 0.840 nm or hexagonal ilmenite structure, a = 0.507 nm) and $Zn_2Ti_3O_8$ (cubic inverse defect spinel, a = 0.843 nm) are still under debate.[27–29]

Instituto de Ciencia de Materiales de Madrid (ICMM-CSIC), Campus de Cantoblanco, 28049, Madrid, Spain. E-mail: caretti@icmm.csic.es; Fax: +34 91 372 0623; Tel: +34 91 334 9000

Despite the extensive studies performed on the individual TZO and ZnO–TiO_2 systems in areas such as photovoltaics, photocatalysis or optoelectronics, there is a lack of systematic work to fully understand Ti incorporation into the ZnO structure either as a dopant or to form a mixed oxide. In particular, one of the current technological challenges is the elucidation of such mechanism for nanostructured and ultrathin films due to the size-dependent electronic and optical properties of these semiconductor materials, as discussed in ref. 30. The scarce structural studies performed on these systems by XANES have used high energy photons to excite the K-edges of Ti and Zn.[17,31] However, it is very informative to study the L-edges because their features are sharper and better resolved. In this work we have performed XANES at the Ti–L, Zn–L and O–K edges to explore the transition among those regimes (doped *versus* mixed oxide) by increasing the Ti load in ZnO films with thicknesses in the 10–40 nm range.

$Ti_{(1-x)}Zn_{2x}O_2$ ($0 \leqslant x \leqslant 1$) samples were prepared by DC reactive magnetron sputtering on high resistivity (>6000 Ω cm) silicon wafers with a (100) orientation. Even though no intentional heating was applied to the substrate, a temperature between 90–100 °C was reached during deposition due to the impinging sputtered atoms, as measured with a thermocouple in contact with the sample. The samples were grown introducing a mixture of Ar (99.999%) and O_2 (99.992%) gases in the vacuum chamber using a relative oxygen gas flow of 20% and a total flow (Ar + O_2) of 30 sccm (standard cubic centimetres per minute). All the samples were prepared after complete poisoning of both cathodes. Firstly, different samples were deposited maintaining the Zn cathode power (P_{Zn}) at 100 W and increasing the Ti cathode power (P_{Ti}) from 0 to 120 W. Secondly, P_{Ti} was maintained at 100 W increasing P_{Zn} from 0 to 100 W. In this way, ultrathin films with thicknesses between 13 and 38 nm were obtained using a constant deposition time of 6 min. Further details on the experimental setup and procedure can be found elsewhere.[32]

For the study of the chemical composition of the films, Rutherford backscattering spectroscopy (RBS) experiments were carried out with the 5 MV HVEE Tandetron accelerator sited at the Centro de Micro-Análisis de Materiales (CMAM) of Universidad Autónoma de Madrid.[33] The RBS experiments were performed using 3.035 MeV He^+ ions to make use of the cross section resonance ^{16}O (α, α) ^{16}O at that particular energy and, therefore, to improve the sensitivity to oxygen. The chemical composition values have been extracted using the RBX software.[34] The X-ray absorption near edge structure (XANES) measurements were done at the PM4 beamline
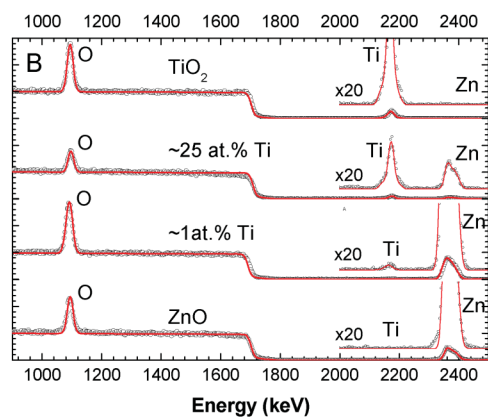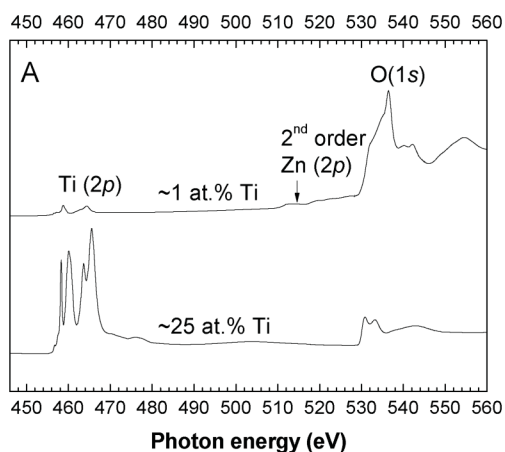
Fig. 1 XANES survey (A) and RBS spectra (B) of samples with $\sim$1 at.% and $\sim$25 at.% of Ti. Reference RBS spectra for TiO_2 and ZnO materials are also included.

of the Bessy II synchrotron facility (Berlin, Germany), using the SurICat endstation. The XANES spectra were recorded in the total electron yield (TEY) mode by registering the current drained to ground from the sample. The latter was normalized to the current from a gold-coated grid located upstream in the X-ray beam path.

Fig. 1 shows the XANES survey and RBS spectra of two selected samples with low (1 at.%) and high (25 at.%) Ti content, which were deposited using relative target powers of $P_{Zn}/P_{Ti} = 100$ W/40 W and 10 W/100 W, respectively (see Table 1). Pure ZnO and TiO_2 reference spectra are also plotted in Fig. 1B for comparison purposes. In

Table 1 RBS and XANES composition of the Ti–Zn–O films

Cathode power P_{Zn}/P_{Ti} (W/W)	RBS (at.%)			XANES (at.%)		
	Ti	Zn	O	Ti	Zn	O
100/10	0.3	45.5	54	0.5	45.9	53.6
100/40	0.9	44	55.1	1.3	40.0	58.7
100/60	1.3	45.5	53.2	0.7	35.3	64.0
100/80	1.5	44	54.5	2.4	36.1	61.5
100/100	1.9	43.6	54.5	3.6	38.2	58.2
100/120	2.4	43.5	54.1	3.1	36.0	60.9
10/100	27.3	16.4	56.3	22.0	27.1	50.9
40/100	6.5	37.8	55.7	6.6	41.4	52.0
60/100	3.7	50.6	45.7	3.2	34.0	62.8
80/100	1.5	44.4	54.1	2.8	39.6	57.6
100/100	1.8	43.6	54.6	3.6	38.2	58.2

Fig. 1A the Ti L and O K-edges are presented, together with zinc's second order signal. Fig. 1B displays the RBS spectra (experimental data and the global fit results) with a zoom out ($\times$20) of the area where the metal elements are observed (E = 2000–2500 keV). Both techniques are suitable to detect low metal contents in the deposited ultrathin films. The quantification of the elemental composition of all samples by XANES and RBS is summarized in Table 1, where the relative target power is also indicated. In general, there is a good agreement between the quantification by both techniques, taking into account that RBS quantifies the whole film, whereas XANES only maps the outermost $\sim$5 nm region.

Fig. 2 shows the variation of the titanium atomic content (%) in the films obtained by XANES (open circles) and RBS (close circles). For the sake of simplicity, we will use the composition as measured by RBS in the discussion of Fig. 2. For the samples deposited with a fixed $P_{Ti} = 100$ W and $P_{Zn} < 60$ W, there is an abrupt decrease of the titanium content from $\sim$30 $\pm$ 1 at.% down to $\sim$4.0 $\pm$ 0.5 at.%. For higher Zn cathode powers the amount of titanium remains fairly constant around 2.0 at.%. In the cases where the samples are deposited with a constant Zn cathode power $P_{Zn} = 100$ W, the titanium content slightly and linearly increases with the Ti cathode power from 0 to 2.4 at.%.

As a whole, regardless of the cathode power, the Ti concentration in the films always stays below 7 at.%, except for the one deposited with $P_{Zn}/P_{Ti} = 10$ W/100 W. The incorporation of Ti in the films is controlled by the very low sputtering rate of Ti compared to Zn. Hence, we observe a significant increase in Ti concentration only for low Zn cathode powers below 40 W. Next, we will elucidate how these changes observed in the composition of the samples are reflected in the bonding structure of the formed compounds.

Fig. 3 shows the XANES spectra of selected $Ti_{(1-x)}Zn_{2x}O_2$ samples for decreasing Ti concentration, from 22 at.% to 0.5 at.%, together with the reference spectra of anatase TiO_2 and wurtzite w-ZnO thin films grown with the same sputtering setup. The composition values indicated correspond to the XANES data of Table 1. The Ti L-edge XANES spectrum of barium orthotitanate (Ba_2TiO_4) and the Zn L-edge XANES spectrum of zinc sulphate ($ZnSO_4$) have been taken from the literature for comparison purposes.[35,36]
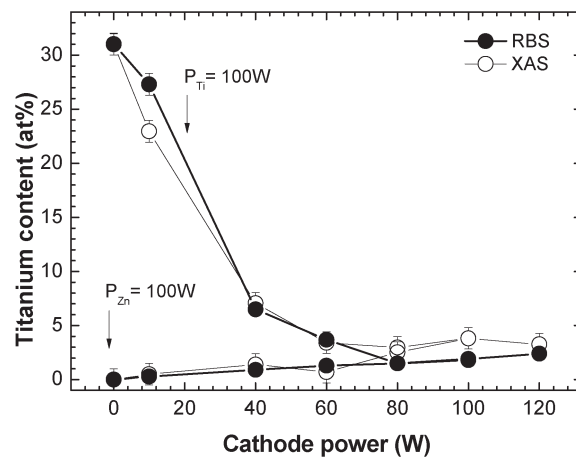
Fig. 2 Variation of the titanium atomic content (at.%) in the Ti–Zn–O thin films with the Zn and Ti cathode powers for a fixed Ti and Zn powers of 100 W, respectively.
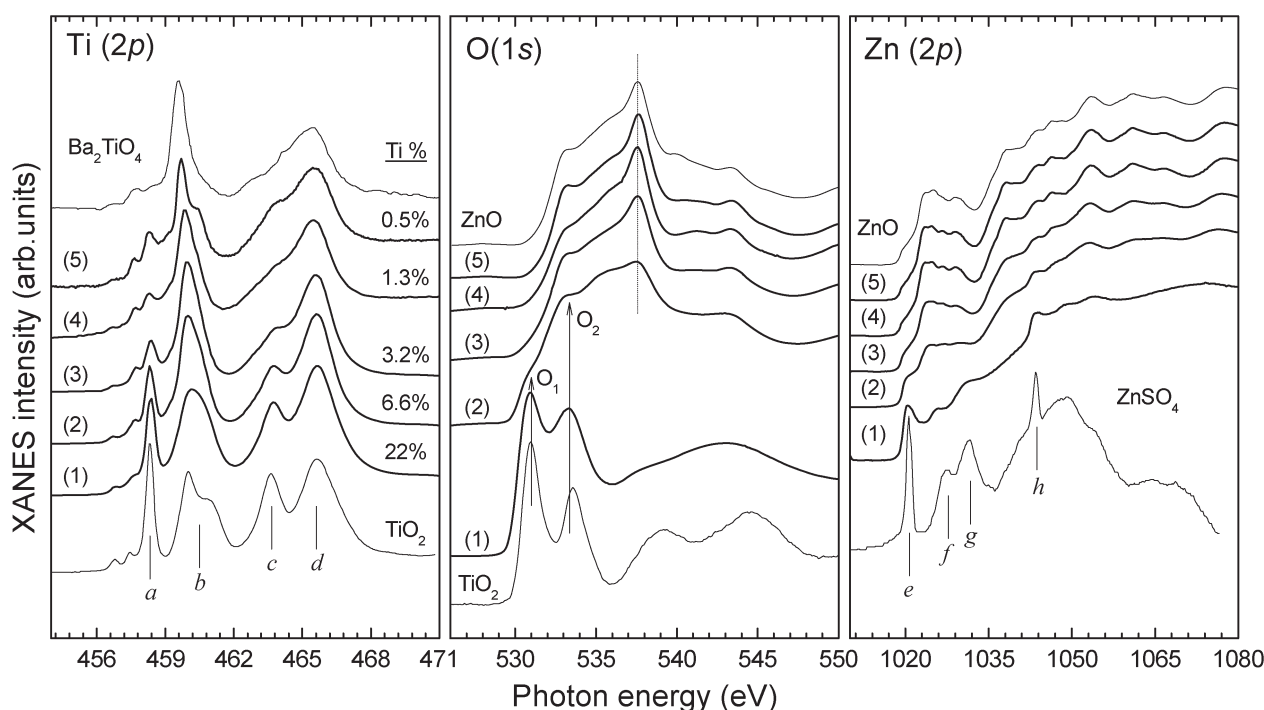
Fig. 3 Ti L-, Zn L- and O K-edge XANES spectra of TZO ultrathin films. Titatium at.% concentrations are indicated as calculated by XANES (see Table 1). Anatase TiO_2 and wurtzite ZnO thin films grown with the same sputtering setup are included, together with the Ti L-edge XANES spectrum of barium orthotitanate (Ba_2TiO_4)[35] and the Zn L-edge XANES spectrum of zinc sulphate $(ZnSO_4)$.[36]

In the case of anatase TiO_2, the Ti L-edge peaks (*a,b*) and (*c,d*) correspond to the (t$_{2g}$, e$_g$) sublevels in the L$_3$- and L$_2$-edges, respectively, where the characteristic peak *b* splitting arises from strong distortion of the Ti^{4+} octahedral symmetry.[37] Spectrum (1) shows that, for a Ti content of 22 at.% in the films, the Ti L-edge is similar to that of pure anatase TiO_2. However, the considerably smaller *b* splitting in sample (1) indicates a higher octahedral symmetry compared to anatase, which is typical of titanate phases.[37] Moreover, the Zn L-edge of spectrum (1) exhibits 4 features distinctive of a zinc sulphate like structure (isostructural to Cu_2SO_4), which are labelled *e–h* in the reference spectrum. Zn^{2+} cations are thus coordinated to oxygen in octahedral symmetry, with a coordination number of 6. These observations suggest that sample (1) has a hexagonal h-$ZnTiO_3$ ilmenite type structure formed by ZnO_6 and TiO_6 octahedrons. Zn L- and O K-edges of zinc spinel compounds[38,39] are completely different to those in spectrum (1), excluding the formation of other known zinc titanate phases with inverse spinel structure (*e.g.* cubic $ZnTiO_3$ or Zn_2TiO_4). Furthermore, the O K-edge line shape is consistent with an ilmenite-like structure.[40] Remarkably, even at this high Zn concentration (27 at.%), the O K-edge XANES contains no w-ZnO signal. A decrease in the separation of peaks O_1 and O_2 compared to anatase TiO_2 indicates a lower crystal field splitting value, as expected for the mentioned reduction of the octahedral distortion in titanates. Curiously, due to their structural similarities, an h-$ZnTiO_3$ like phase should generally be obtained from a rutile TiO_2 precursor and not anatase (the phase obtained here without Zn sputtering).[41]

For a considerably lower Ti content of 6.6 at.% (spectrum (2)), the Zn L-edge XANES spectrum is now quite similar to w-ZnO, but still exhibits weak hints of the *e–h* features from ZnO_6 octahedrons.

Besides, the significant narrowing and a downwards energy shift of peak *b* in the Ti L-edge of spectrum (2) points to a further reduction of the octahedral distortion and of the resulting crystal field splitting (related to the *a–b* peak separation).[37] Again, these changes are characteristic of the Ti L-edge XANES spectrum of a titanate compound containing TiO_6 units. Regarding the O K-edge, clear contributions from both w-ZnO and TiO_6 environments are observed, what indicates the formation of a mixed oxide structure. Hence, we assign spectrum (2) to the formation of a w-ZnO/h-$ZnTiO_3$ mixed-phase oxide.

Further reduction of the Ti concentration produces a significant intensity reduction of peaks *a* and *c* in the Ti L-edge XANES of samples (3) to (5). Additionally, peak *b* keeps narrowing and shifting to lower photon energies. These changes are explained by a gradual modification of the Ti site geometry from octahedral to tetrahedral symmetry and the consequent reduction in the coordination number from 6 to 4. The same transformation has been reported for the Ti L-edge XANES spectra of $BaTiO_3$ (octahedral symmetry) and Ba_2TiO_4 (tetrahedral symmetry).[35] At this point, we cannot entirely exclude the formation of a 5-coordinate square pyramidal Ti species (*e.g.* a fresnoite structure[42]) in this transition from high to low Ti content in the TZO films. The Zn L- and O K-edges of spectra (3)–(5) are almost identical and characteristic of w-ZnO (see reference spectrum). Moreover, as in pure ZnO, samples (3)–(5) reveal a dominant O peak at ~537.5 eV from transitions to O $2p_z$ and O $2p_{x+y}$ states,[43] which is indicative of O-terminated surfaces.[44] Thus, the XANES results indicate that for Ti concentrations below 3 at.% the Ti atoms incorporate in the ZnO structure with tetrahedral symmetry by substituting the Zn^{2+} cations in the oxide lattice, that is, forming a Ti-doped

w-ZnO phase. Interestingly, we observe again a splitting of peak *b* for the lowest Ti concentration (0.5 at.%) that may be related with a distortion of the tetrahedral Ti^{4+} coordination symmetry due to differences in the Ti–O and Zn–O bond distances.

A preliminary study of the electrical properties of the TZO films was carried out with the four-point probe method. As reference value, the undoped ZnO sample has a resistivity of 1.52 Ω cm. Interestingly, the TZO coating with a 0.5 at.% Ti concentration gave the lowest resistivity of $4.5 \times 10^{-2} \Omega$ cm for our samples. Thus, the optimum behaviour of Ti as an electrical dopant takes place for concentrations below 1 at.%. A similar behaviour, but with a Ti load threshold of 1.3 at.%, has been reported for 500 nm[16] and 650 nm[17] thick TZO films, with optimum resistivities of $9.02 \times 10^{-3} \Omega$ cm and $3.82 \times 10^{-3} \Omega$ cm, respectively. TZO resistivity values found in the literature[13–17] are generally smaller than the ones reported in this communication for ultrathin TZO films, whose significantly lower thickness may result in increased resistance values due to larger electron scattering effects. In fact, an increase of one order of magnitude in the resistivity has been described for decreasing thicknesses of TZO coatings from 950 nm to 30 nm.[14] Our resistivity measurements are comparable to the 30 nm thick TZO in ref. 14 and to recently reported Ti doped ZnO nanowires.[45] At this stage, we have not identified the type and concentration of defects present in our samples. Therefore, we have decided to avoid any speculative arguments concerning the defect chemistry and its connection to the conduction mechanisms in TZO.

According to the above, ZnO samples doped with a 0.5 at.% of Ti and thicknesses down to 10 nm may be suitable for electronic and optoelectronic devices, solar cells, photoelectrodes, photocatalysts or sensors.

Conclusions

Ultrathin films with $Ti_{(1-x)}Zn_{2x}O_2$ ($0 < x \leqslant 1$) compositions were deposited at room temperature by DC reactive magnetron sputtering on (100) Si wafers. We observe a transition from octahedrally coordinated Zn^{2+} in a h-$ZnTiO_3$ like structure to the expected tetrahedral symmetry in the w-ZnO matrix of TZO films. Regarding Ti^{4+}, a similar change from octahedral to tetrahedral sites is detected in the transition from h-$ZnTiO_3$ to TZO coatings. Therefore, Ti is incorporated as a dopant by substituting Zn atoms in the wurtzite ZnO structure. The optimum Ti doping was found to be 0.5 at.%, for which the TZO sample showed a much lower resistivity than the more insulating ZnO films.

Acknowledgements

References

1 K. Ellmer and A. Klein in *Transparent Conductive Zinc Oxide: Basics and Applications in Thin Film Solar Cells*, ed. K. Ellmer, A. Klein, B. Rech, Springer, New York, 2008, ch. 1, 1–27.
2 T. Minami, *MRS. Bull.*, 2000, **25**, 38.
3 T. Kamiya and M. Kawasaki, *MRS Bull.*, 2008, **33**, 1061.
4 H. Ohta and H. Hosono, *Mater. Today*, 2004, **7**, 42.
5 A. Anders, S. H. N. Lim, K. M. Yu, J. Andersson, J. Rosén, M. McFarland and J. Brown, *Thin Solid Films*, 2010, **518**, 3313.
6 S. Cornelius, M. Vinnichenko, N. Shevchenko, A. Rogozin, A. Kolitsch and W. Möller, *Appl. Phys. Lett.*, 2009, **94**, 042103.
7 C. G. Granqvist, *Sol. Energy Mater. Sol. Cells*, 2007, **91**, 1529.
8 K. Ellmer, *J. Phys. D: Appl. Phys.*, 2001, **34**, 3097.
9 H. C. Park, D. Byun, B. Angadi, D. Hee Park, W. K. Choi, J. W. Choi and Y. S. Jung, *J. Appl. Phys.*, 2007, **102**, 073114.
10 M. Gabas, P. Diaz-Carrasco, F. Agullo-Rueda, P. Herrero, A. R. Landa-Canovas and J. R. Ramos-Barrado, *Sol. Energy Mater. Sol. Cells*, 2011, **95**, 2327.
11 D. H. Chi, L. T. Thanh Binh, N. Thanh Binh, L. D. Khanh and N. N. Long, *Appl. Surf. Sci.*, 2006, **252**, 2770.
12 Z. L. Tseng, P. C. Kao, C. S. Yang, Y. D. Juang, Y. M. Kuo and S. Y. Chu, *J. Electrochem. Soc.*, 2011, **158**, J133.
13 Y. M. Lu, C. M. Chang, S. I. Tsai and T. S. Wey, *Thin Solid Films*, 2004, **447–448**, 56.
14 H. P. Chang, F. H. Wang, J. C. Chao, C. C. Huang and H. W. Liu, *Curr. Appl. Phys.*, 2011, **11**, S185.
15 F. H. Wang, H. P. Chang and J. C. Chao, *Thin Solid Films*, 2011, **519**, 5178.
16 J. L. Chung, J. C. Chen and C. J. Tseng, *J. Phys. Chem. Solids*, 2008, **69**, 535.
17 J. J. Lu, Y. M. Lu, S. I. Tasi, T. L. Hsiung, H. P. Wang and L. Y. Jang, *Opt. Mater.*, 2007, **29**, 1548.
18 Y. R. Park and K. J. Kim, *Solid State Commun.*, 2002, **123**, 147.
19 D. Qian, L. Gerward and J. Z. Jiang, *J. Mater. Sci.*, 2004, **39**, 5389.
20 Y. Guim, Sh. Li and Ch. Li, *Microelectron. J.*, 2008, **39**, 1120.
21 M. R. Vaezi, *J. Mater. Process. Technol.*, 2008, **205**, 332.
22 F. Grasset, G. Starukh, L. Spanhel, S. Ababou-Girard, D. S. Su and A. Klein, *Adv. Mater.*, 2005, **17**, 294.
23 A. Dodd, A. McKinley, T. Tsuzuki and M. Saunders, *J. Alloys Compd.*, 2010, **489**, L17.
24 J. S. Jung, Y. H. Kim, S. K. Gi and D. H. Kangl, *J. Electroceram.*, 2009, **23**, 272.
25 Y. C. Lee, Y. L. Huang, W. H. Lee and F. S. Shieu, *Thin Solid Films*, 2010, **518**, 7366.
26 L. Shi, H. Shen, L. Jiang and X. Li, *Mater. Lett.*, 2007, **61**, 4735.
27 Z. Liul, D. Zhou, S. Gong and H. Li, *J. Alloys Compd.*, 2009, **475**, 840.
28 N. T. Nolan, *Chem. Mater.*, 2011, **23**, 1496.
29 T. Ivanova, A. Harizanova, T. Koutzarova and B. Vertruyen, *J. Non-Cryst. Solids*, 2011, **357**, 2840.
30 N. I. Kovtyukhova, E. V. Buzaneva, C. C. Waraksa, B. R. Martin and T. E. Mallouk, *Chem. Mater.*, 2000, **12**, 383.
31 Z. Yong, T. Liu, T. Uruga, H. Tanida, D. Qi, A. Rusydi and A. T. S. Wee, *Materials*, 2010, **3**, 3642.
32 E. Forniés, R. Escobar Galindo, O. Sánchez and J. M. Albella, *Surf. Coat. Technol.*, 2006, **200**, 6047.
33 A. Climent-Font, F. Pászti, G. García, M. T. Fernández-Jiménez and F. Agulló, *Nucl. Instrum. Methods Phys. Res., Sect. B*, 2004, **219–220**, 400.
34 E. Kotai, *Nucl. Instrum. Methods Phys. Res., Sect. B*, 1994, **85**, 588.
35 R. Brydson, L. A. J. Garvie, A. J. Craven, H. Sauer, F. Hofer and G. Cressey, *J. Phys.: Condens. Matter*, 1993, **5**, 9379.
36 G. Nehme, R. Mourhatch and P. B. Aswath, *Wear*, 2010, **268**, 1129.
37 F. M. F. de Groot, J. C. Fuggle, B. T. Thole and G. A. Sawatzky, *Phys. Rev. B: Condens. Matter*, 1990, **41**, 928.
38 R. Revel, D. Bazin and A. M. Flank, *J. Synchrotron Radiat.*, 1999, **6**, 717.
39 W. Sigle, *Annu. Rev. Mater. Res.*, 2005, **35**, 239.
40 R. Brydson, H. Sauer, W. Engel and F. Hofer, *J. Phys.: Condens. Matter*, 1992, **4**, 3429.
41 A. I. Sheinkman, F. P. Sheinkman, I. P. Dobrovol'skii and G. R. Zvyagina, *Izv. Akad. Nauk SSSR Neorg. Mater.*, 1977, **13**, 1447.
42 J. M. Charnock, C. M. B. Henderson, J. F. W. Mosselmans and R. A. D. Pattrick, *Phys. Chem. Miner.*, 2002, **29**, 32.
43 J.-H. Guo, L. Vayssieres, C. Persson, R. Ahuja, B. Johansson and J. Nordgren, *J. Phys.: Condens. Matter*, 2002, **14**, 6969.
44 M. Jullien, D. Horwat, F. Manzeh, R. Escobar Galindo, Ph. Bauer, J. F. Pierson and J. L. Endrino, *Sol. Energy Mater. Sol. Cells*, 2011, **95**, 2341.
45 L. W. Chang, Y. C. Sung, J. W. Yeh and H. C. Shih, *J. Appl. Phys.*, 2011, **109**, 074318.